Doped tin oxide aerogels as oxygen evolution reaction catalyst supports

Lluís Solà-Hernández, Fabien Claudel, Frédéric Maillard, Christian Beauger

Doped tin oxide aerogels as Oxygen Evolution Reaction catalyst supports.

Lluís Solà-Hernández[1,*], Fabien Claudel[2], Frédéric Maillard[2] and Christian Beauger[1,*]

[1] MINES ParisTech, PSL University, Center for Processes, Renewable Energy and Energy Systems (PERSEE), CS 10207 rue Claude Daunesse, F-06904, Sophia Antipolis Cedex, France

[2] Univ. Grenoble Alpes, Univ. Savoie Mont Blanc, CNRS, Grenoble INP, LEPMI, 38000 Grenoble, France

Keywords: Tin dioxide; Aerogel; doping; Iridium Catalyst Support; Oxygen Evolution Reaction; PEM Water Electrolyzers.

Abstract

Designing low cost, highly-active and stable oxygen evolution reaction (OER) catalysts for Proton Exchange Membrane Water Electrolysers (PEMWE) anodes is an important topic for industry and academia. A possible strategy to alleviate the cost of the anodic catalyst consists in synthesizing nanometre-sized catalysts and dispersing them on an electron-conducting and highly-porous support such as SnO_2 doped with hypervalent cations such as Sb(V) and Ta(V). Herein, we show the benefits of Sb- and Ta- doped SnO_2 aerogels synthesized by a sol-gel route. Iridium oxide (IrO_x) nanoparticles were deposited onto SnO_2, SnO_2:Sb and SnO_2:Ta aerogel supports by chemical reduction. The effect of the dopant nature on the aerogel's properties (as morphology, structure, conductivity, etc.) was investigated using a set of physical and chemical techniques. The electrocatalytic performance of the synthesized nanocatalysts towards the OER was also assessed in rotating disk electrode (RDE). Supported IrO_x catalysts showed both higher specific and mass activity and stability than unsupported IrO_x nanoparticles.

Introduction

Polymer Electrode Membrane Water Electrolysers (PEMWE) are attractive devices for hydrogen production from sustainable and clean energy sources such as solar or wind energy.[1,2] Materials challenges in these systems are huge, especially at the anode where the catalyst should be able to face high electrochemical potential (E > 1.6 V *vs*. the standard hydrogen electrode - SHE), highly-acidic environment, presence of oxygen and moderate temperature (< 80 °C), and to electrocatalyze in a sustainable manner the oxygen evolution reaction (OER). Former studies have established that ruthenium oxide (RuO_2) and iridium oxide (IrO_2), two precious metals, are best electrocatalyzing the OER.[3] However, they are presently used in the form of micrometre-sized particles, and typical anode loadings range between 2.0 and 4.0 mg cm^{-2} in present PEMWE anodes, hence a reduction of the Ir content would be highly desirable.[4,5,6,7] One possibility to decrease the catalyst loading consists in using nanometre-sized Ru or Ir catalysts supported on high surface area and electron conducting supports.[8,9] High surface area carbon blacks (CBs) is a popular and widely used support material in electrochemistry, due to its low cost, high specific surface area and high electrical conductivity[10,11,12]. However, CBs face corrosion issue at PEMWE anode potential, thus leading to sintering [13,14,15] and detachment of the noble-metal nanoparticles (NPs), and resulting in depreciated electrocatalytic performance.[16,17,18,19] So far, carbon based materials displaying stability under the required potential for the OER have not been found.[20,21,22] On the contrary, metal oxides feature excellent corrosion resistance and may exhibit strong interactions with the noble metal catalysts.[23,24,25]

In particular, titanium based oxides have received many attention due to their interesting properties. For example, Wang *et al.* obtained an improved Ir utilization compared to the commercial Ir-black by deposition of metallic Ir(0) nanoparticles (NPs) on Ti_4O_7 without any thermal treatment.[26] Chen and co-workers also demonstrated enhanced OER activity in acid media when using Ti_4O_7 as an Ir catalyst support.[27] Siracusano *et al.* also obtained better performances when depositing IrO_2 electrocatalysts on Ti based suboxides.[28]

Tin oxide doped based materials have also shown promising stability under OER conditions, as for example Indium doped (ITO)[29] or Antimony doped (ATO).[30,31,32,33] A highly active OER catalyst consisting of $IrNiO_x$ supported on mesoporous ATO has been developed by the Strasser's group. The authors reported improved OER activity and stability, which was accounted for by a Metal-Metal Oxide Support Interaction (MMOSI) between the amorphous IrO_x catalyst and the supporting material.[9,34] Wang and co-workers [35] also reported enhanced OER activity and stability of Ir catalysts supported onto ATO aerogels.[36] However, Claudel *et al*. recently reported that stability of the doping element is a key issue for ATO to be implemented in PEMWE anode.[19] Ta-

doped SnO_2 supports (TaTO) have been first used by Senoo *et al.* as a catalyst support at a proton-exchange membrane fuel cell (PEMFC) cathode. The authors demonstrated enhanced catalytic performance toward the oxygen reduction reaction (ORR) and improved corrosion resistance for Pt/SnO_2:Nb *vs.* Pt/CB.[37,38] Fabbri *et al.* also demonstrated superior ORR activity of Pt NPs deposited on Ta-, Nb- and W-doped SnO_2 relative to Pt/glassy carbon.[39] Uchida *et al.* reported improved utilization of Ir atoms in Ir/TaTO catalysts used at a PEMWE anode.[40]

Herein, SnO_2 (TO), SnO_2:Ta (TaTO) and SnO_2:Sb (ATO) aerogels with three-dimensional texture, amenable morphology, and tuneable electronic conductivity (via doping) were synthesized, decorated with partially oxidized iridium oxide (IrO_x) NPs and tested in simulated PEMWE electrolyser conditions.

2. Experimental

2.1 Synthesis and preparation of the alkoxide precursor ($Sn(OiPr)_4$)

A tin metal alkoxide precursor ($Sn(OiPr)_4$) was first prepared using the procedure described in Thomas *et al.*[41] In brief, 3.7 mL of tin tetrachloride ($SnCl_4$) were added into a 500 mL dry reactor flask under inert atmosphere with 50 mL of previously dried and degassed heptane. After 10 minutes of stirring at room temperature, a solution of 17 mL of diethylamine dissolved in 20 mL of dried heptane was added by using a syringe in order to keep the inert atmosphere, and then the reaction was kept under stirring for 2 hours. After that, a 17 mL solution of *tert*-butanol dissolved in 70 mL of dried heptane was added to the reactor and kept under stirring for 72 hours. The product was then filtered inside an inert atmosphere glove box and the filtrate was washed several times with heptane. 30 mL of dried isopropanol were added to the filtrate, and the reaction was kept under stirring and inert atmosphere for 24 hours more. Finally the solution was evaporated under vacuum in order to eliminate non desirable by-products and solvents, and the obtained alkoxide was re-diluted with the desired amount of isopropanol in order to obtain a solution of $Sn(OiPr)_4$ at 10% mass in volume (total yield = 40%).

2.2 Aerogels preparation by the sol-gel route

Doped and un-doped TO aerogels with high surface area were synthetized by the sol-gel method, previously reported by our group,[37] using alkoxide precursors. Two solutions (A & B) were prepared. Solution A, consisting of tin isopropoxide ($Sn(OiPr)_4$) dissolved in isopropanol and the corresponding amount of the antimony alkoxide precursor as doping element ($Ta(OiPr)_5$ or ($Sb(OiPr)_3$, Across Organics), were mixed under magnetic stirring. Solution B, consisting of nitric acid (Alfa Aesar, 2M) as the sol-gel reaction catalyst (Cat/Sn = 0.072) and water (H_2O/Sn = 3.06 mol/mol) were diluted in isopropanol and mixed under magnetic stirring.

Solution B was then slowly added into solution A and a gel formed after a few minutes. Then the gels were covered with 10 mL of isopropanol (to prevent drying), and aged for 72 hours at room temperature before being washed with isopropanol three times a day for three days. Once washed, the resulting gels were dried under CO_2 in supercritical conditions (80 bars, 40 °C) to obtain amorphous aerogels. After calcination under air at 600°C, the ATO aerogels turned blue, while TaTO aerogels remained white.

2.3 Deposition of IrO_x nanoparticles by chemical reduction

IrOx NPs were deposited onto the aerogel supports using the procedure previously described by Wang *et al*.[36] In brief: 1.17 g of cetyltrimethylammonium bromide (CTAB, Merck Millipore), 0.095 g of as-prepared TO, ATO or TaTO aerogel and 0.075 g of the Ir precursor ($IrCl_3$, Sigma Aldrich) were dispersed in a 120 mL anhydrous ethanol solution (VWR Chemicals) and magnetically stirred for 4 hours under an argon (Ar) atmosphere. To reduce Ir^{3+} ions, 0.114 g of sodium borohydride ($NaBH_4$, Sigma Aldrich) were dissolved in 50 mL of anhydrous ethanol, and the resulting solution was added slowly to the first reaction suspension under vigorous stirring and Ar atmosphere. The reaction mixture was kept for 4 hours until the reduction reaction completed. Afterwards, the suspension containing Ir/TO-based support was centrifuged and rinsed with ample amounts of pure ethanol and deionized water to remove CTAB and the residual non-reduced $IrCl_3$. Finally, the synthesized catalyst was dried overnight at 80°C under air atmosphere. The nominal Ir loading was 30 wt. %.

2.4 Materials Characterization

X-ray diffraction (XRD) analyses were performed using an X'Pert pro-Philips diffractometer (Cu Kα of λ = 1.5405 Å), operating at 45 kV and 30 mA. Data were collected from 20° to 90° in 2-θ mode with a Pixcel counter. The crystallites size was determined using the Debye-Scherrer method and the (111) diffraction peak.

The morphology of the synthesized aerogels was determined using a Supra 40 scanning electron microscope (SEM) equipped with a Gemini column, and operated at 3.00 kV. Samples were deposited onto adhesive conducting carbon tapes and coated with a 7 nm thick platinum layer, using a Quorum (Q150 T).

Transmission electron, microscopy (TEM) measurements were performed using a JEOL 2010 operated at 200 kV (point-to-point resolution of 0.19 nm).

Nitrogen sorption analyses were performed with a Micromeritics ASAP 2020. Before analyses, samples were degassed for 120 min at 100 °C and 10 µm Hg. For specific surface area determination, the Brunauer-Emmett-Teller (BET) model was applied. The pore size distributions were determined by applying the Barret-Joyner-Halenda (BJH) method to the desorption branch of the isotherms. The *t*-plot construction using Harkins-Jura

correlation was used for microporosity assessment. We assumed that the calcined samples were mechanically strong enough to withstand the pressure applied during the measurement.

The bulk chemical compositions of the samples was determined by Energy Dispersive X-ray Spectroscopy (EDX) during SEM observations with a Philips XL30 operated at 15 kV.

Insights into the near-surface chemical composition were obtained by X-ray Photoelectron Spectroscopy (XPS) using a Thermo Scientific K-Alpha system. The spectrometer was equipped with a monochromatic Al *K*α source and a low energy flood-gun for charge compensation. The ellipsoid spot size is about 350 µm x 700 µm.

The electronic conductivity of the synthesized aerogels was determined with a homemade conductivity cell, made up of two copper electrodes (S = 0.785 cm²) surrounded with a Teflon ring. Approximatively 100 mg of sample were introduced between these two electrodes (see **Figure 1**). A potentiostat was used to apply a current of 100, 150, 250 and 400 mA and the voltage was measured for each current. The homemade conductivity cell was placed in a press and measurements were made at room temperature with 1 ton of pressure. The conductivity (σ, S/cm) was calculated with the formula $\sigma = (e.I/U.S_{electrode})$ where "*e*" is the thickness of the sample (cm), "*I*" the applied current (mA), "$S_{electrode}$" the surface of the electrode (cm^2) and "*U*" the measured voltage (mV).

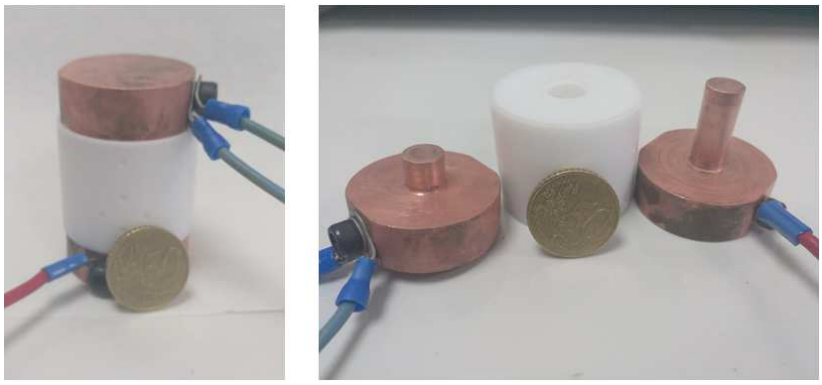

Figure 1: Homemade conductivity cell picture assembled (left) and disassembled (right)

The electrochemical measurements were performed with an Autolab PGSTAT20 potentiostat and a rotating disk electrode (RDE). Inks were prepared by mixing a given mass of the synthesized catalysts, a 5 wt. % Nafion® solution, isopropanol and ultrapure water. An aliquot of 10 µL of the catalyst suspension was deposited on the working electrode (glassy carbon disk, geometric area: 0.196 cm²) by spin coating, targeting a final loading of 20 $\mu g_{Ir}\ cm^{-2}_{geom}$. The counter electrode was a Pt foil and the reference electrode a Reversible Hydrogen Electrode (RHE). The OER evaluation tests were performed in N_2-saturated 0.05 M H_2SO_4 using a rotating speed of 1600

revolutions per minute (rpm). The sequence test described in **Table 1** was used for electrochemical characterization and determination of the OER activity.

Table 1. Sequence used for electrochemical characterizations

Sequence Number	Starting Potential (V *vs*. RHE)	Potential range (V *vs*. RHE)	Sweep rate (mV s^{-1})	N° Cycles	Purpose
1	1.0	1.0 – 1.6	5	3	OER pre-test
2	OCP	0.0 – 1.6	20	10	Electrochemical conditioning
3	1.0	1.0 – 1.6	5	3	OER activity evaluation
4	Chronopotentiometry at 1 mA.cm^{-2} for 24 hours				Stability test

The current obtained at 1.51 V (η = 0.28V) in the last sequence step, was normalized either by the mass of Ir initially deposited on the electrode (j_{mass}) or by the anodic charge measured between 0.40 and 1.40 V *vs.* RHE, which is known to be proportional to the amount of Ir oxide (j_{spec}).[42,43]

3. Results and discussion

3.1 Aerogels characterization

Antimony-doped (ATO), Tantalum-doped (TaTO) and un-doped (TO) tin oxide aerogels were prepared by the sol-gel route described in the Experimental Section.

Structure and morphology of aerogels

The morphology and the structure of the as-prepared aerogels were characterized by SEM, nitrogen sorption measurements and XRD. **Figure 2a** shows the characteristic XRD peaks, (110), (101), (200), (211), (200), of the rutile structure of TO. No peak corresponding to Sb or Ta phases (SnO, or M, MO, M_2O_3, M_2O_5 with M = Sb or Ta) was found, indicating that the dopant atoms substituted Sn atoms or are inserted randomly in the rutile network. Moreover, as shown in **Table 2**, the "*a*" and "*c*" lattice parameters of TaTO or ATO aerogels are

unchanged compared to pure TO, suggesting no deformation of the rutile cell of TO. The XRD patterns displayed in **Figure 2a** and the crystallite sizes evaluated using the Debye-Scherer equation (**Table 2**) nevertheless show that the doped aerogels are less crystalline and feature smaller crystallites than the pure TO material. SEM images displayed in **Figure 2(c-e)** show that aerogels feature an airy morphology lying on a three-dimensional network composed of interconnected primary particles with size comprised between 15 and 20 nm (**Table 2**). This morphology is similar to that of carbon and SnO_2 based aerogels previously synthesized by our group.[44] The agglomeration of the primary particles leads to pores of different sizes: micropores (< 2 nm), mesopores (2 < size < 50 nm) and macropores (50 nm).

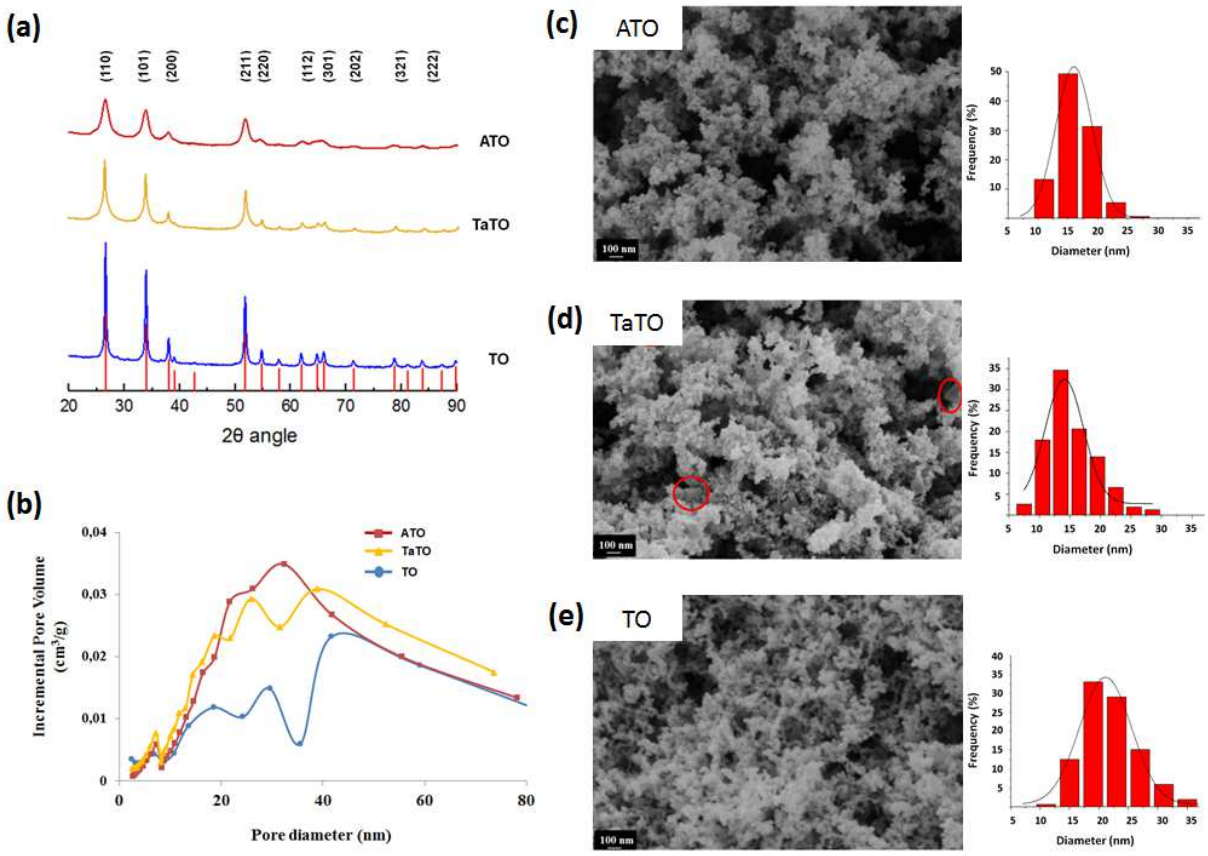

Figure 2: X-ray diffraction patterns (a), pore size distribution (b), SEM images (Magnification of the images = 50000 X) and associated primary particle size distributions (c) for pure and doped SnO_2 aerogels (Red bars in (a) correspond to the pattern of the rutile structure of tin oxide [45] JCPDS 14-1445).

The mean crystallite size and the mean primary particle size determined by SEM (150 particles were analysed using Image J) are displayed in **Table 2**. For the doped samples, we observed that the primary particle size systematically exceeds the crystallite size, suggesting that the aerogel is polycrystalline. Importantly, we also noticed that large and small particles co-exist inside the TaTO aerogel (**Figure 2d**). Local EDX analyses

indicated that the large particles are depleted in Ta, and such domains are believed to be responsible of the higher degree of crystallinity of TaTO *vs*. ATO. In contrast, the crystallite and particle sizes are similar for the un-doped aerogels (**Figure 2e)**, suggesting a monocrystalline material.

Table 2. "*a*" and "*c*" lattice parameters and crystallite size determined by XRD and primary particles size (SEM) of doped and un-doped samples.

Sample	***a* // *c* lattice parameters (nm)**	**Crystallite size (nm)**	**Primary particle size (nm)**
TO	4.7 // 3.2	23.0	22.1 ± 5.1
ATO	4.7 // 3.2	5.1	16.3 ± 2.8
TaTO	4.7 // 3.2	8.2	15.4 ± 4.1

Nitrogen sorption measurements were performed (**Figure 2b** and **Table 3)** to determine the textural properties of the synthesized aerogels. All measured isotherms indicated mesoporous materials, and this was confirmed by the specific surface area values (**Table 3**) and the pore size distributions (PSD, **Figure 2b**) calculated based on the BET and BJH models, respectively. The presence of mesoporosity is key to efficiently deposit IrO_x NPs within the aerogel and thus ensure higher mass activity towards the OER. **Figure 2b** reveals a multimodal pore size distribution centred at 20 and 40 nm for all synthesized aerogels. However, due to smaller primary particles, higher specific surface area was measured for the doped aerogels.

Table 3. Nitrogen sorption measurement results for doped and pure SnO_2 aerogels.

Sample	**Specific surface area BET ($m^2\ g^{-1}$)**	**PSD (BJH, nm)**	**Pore volume (BJH, $cm^3\ g^{-1}$)**	**µ-pore volume (BJH, $cm^3\ g^{-1}$)**
TO	41.1	20 — 30 — 40	0.059	0.4×10^{-2}
ATO	76.9	20 — 25 — 35	0.295	0.9×10^{-2}
TaTO	74.6	20 — 25 — 40	0.293	0.1×10^{-2}

Aerogel chemical composition

It is well-established that the electronic conductivity strongly depends on the nature and the content of the doping element as well as the homogeneity of doping [37,46,47,48,49,50,51]. During the synthesis of the TO-based aerogels, elements may segregate during the sol-gel process or during the calcination step. To determine the homogeneity of doping in ATO and TaTO aerogels, the bulk and the near-surface chemical compositions were determined by EDX and XPS, respectively. Some difficulties arised to quantify the Sb content by XPS, as the most intense peak of Sb (Sb 3d5) is located at the same binding energy than the O 1s peak (≈ 530 eV). To avoid interferences, the Sb content was determined using the less intense Sb 3d3 peak at *ca*. 540 eV (**Figure 3**). For determination of the near-surface composition of TaTO, the Ta 4d5 and Ta 4d3 peaks were used.

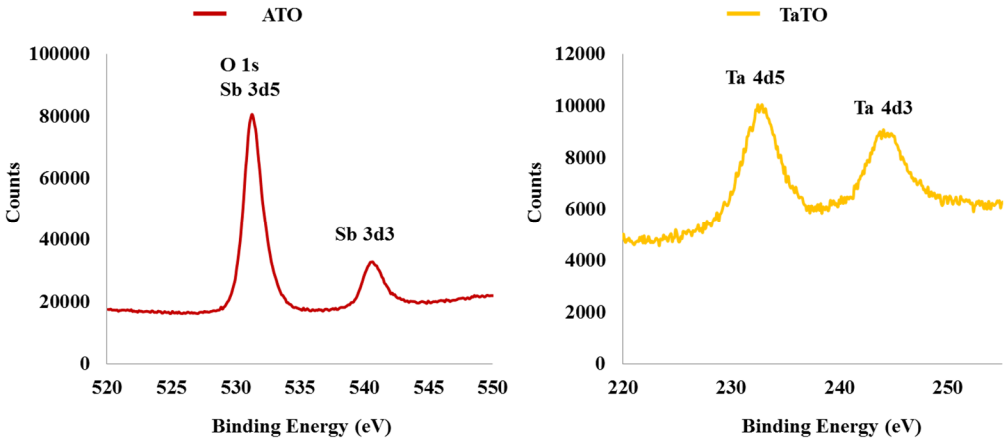

Figure 3. XPS spectra focusing on Sb3d (left) and Ta 3d5/3d3 (right)

According to EDX measurements (**Table 4**), the bulk concentration of the doping element was 12 at. % for ATO and 14 at. % for TaTO (nominal value 10 at. %). The near-surface Sb content in ATO measured by XPS was found notably higher than the bulk concentration (15 at. % *vs* 12 at. %), in agreement with former results.[37] Similarly, the Ta concentration was found higher in the near-surface region of the aerogel than in the bulk (16 at. % *vs* 14 at. %). Despite results obtained by EDX and XPS should be regarded semi-quantitative, we believe that the observed trend is significant. Surface and near-surface enrichment by the doping element can be attributed to interatomic diffusion during the calcination step. Different kinetics of hydrolysis or condensation of the used precursors, represent another possibility to account for these results. Segregation of the doping element represents a significant pitfall in terms of electronic conductivity and can be mitigated, for example by selecting other sol-gel precursors with similar hydrolysis/condensation kinetics than those of the Sn precursor.

Table 4. Bulk and near-surface chemical composition of the as-prepared aerogels determined by EDX and XPS analyses.

Sample	Dopant/(Dopant + Sn) EDX (at.%)	Dopant/(Dopant + Sn) XPS (at.%)
TO	-	-
ATO	11.8 ± 2.5	14.9 ± 0.1
TaTO	14.0 ± 1.9	16.1 ± 0.4

Electronic conductivity measurements

As seen in **Table 5**, Ta is much less efficient than Sb to enhance the electronic conductivity of the TO aerogels. Indeed, while a four orders of magnitude enhancement was reached with 12 at. % of Sb, a modest 3-fold enhancement of the electronic conductivity was achieved upon doping the TO aerogel with 14 at. % of Ta, in agreement with former reports in the literature. Despite optimal doping rates depend on the nature of the element,[39] we purposely kept similar values for ATO and TaTO so as not to impact the morphology of the support and allow a straightforward comparison between the different samples.

Table 5. Aerogels conductivity determined by resistance measurements obtained with an applied pressure of 1 ton.

Sample	Conductivity (S cm^{-1})
TO	5×10^{-4}
ATO	8.2×10^{-2}
TaTO	17×10^{-4}

The electronic conductivity is also known to depend on both the charge carriers' concentration and their mobility, the latter being notably influenced by grain and domain boundaries.[48] Since ATO and TaTO samples synthesized in this study feature similar particle sizes, we believe that the density of grain boundaries is similar for both materials. Hence, the higher conductivity observed for ATO most likely results from a higher charge

carrier's density, in agreement with former claim of Bruneaux *et al.*[52] This may be rationalized by considering different possible oxidation states for Sb. As already discussed [37], the valency of the doping element will determine the concentration of oxygen vacancies hence the electronic conductivity.

3.2 IrO_x/Aerogel characterization

IrO_x NPs were deposited onto the different aerogels using a chemical route (see section 2.4 of Experimental for details). As revealed by **Figure 4**, these IrO_x NPs feature a face-centred cubic structure. Because the synthesis was performed at low temperature and in air-free atmosphere, we did not observe typical reflections of IrO_2.

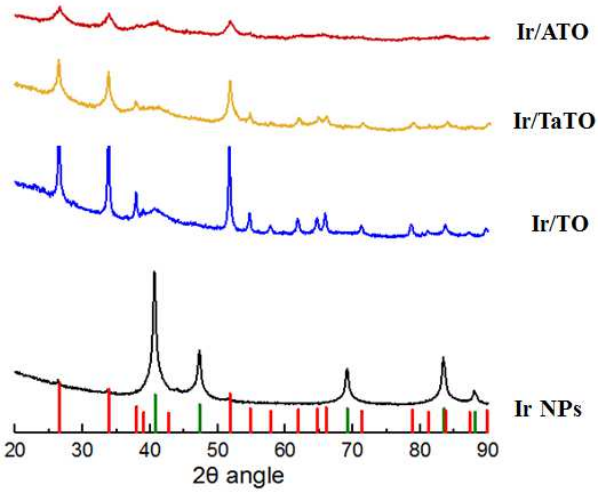

Figure 4. X-ray diffractograms of Ir NPs (black), Ir/TO (blue), Ir/ATO (dark red) and Ir/TaTO (yellow). Red bars correspond to the rutile structure of pure TO and green color ones correspond to Ir(0) pattern.[46, 53]

TEM images of unsupported and aerogel-supported IrO_x NPs are displayed in **Figure 5**. The IrO_x particle and crystallite sizes were similar for the aerogels-supported IrO_x NPs, reflecting the fact that agglomerate-free single crystalline nanoparticles were deposited onto the TO-based aerogels (**Table 6**). On the contrary, the particle and crystallite size strongly differed for the un-supported IrO_x NPs, providing evidence of a highly polycrystalline material.

EDX and XPS analyses were used to gain insights into the weight fraction (wt. %) and the valency of Ir atoms in each catalyst (**Table 7**). The Ir wt. % determined by EDX was close to the nominal value (30 wt.%), thus

reflecting that the vast majority of the $IrCl_3$ salt was reduced and deposited on each support material. For Ir detection, the peak at 9.17 eV (IrLα emission) was selected, due to the overlapping of the peak at 1.98 eV with the Pt loading signal.

Table 6. Crystallite and particle sizes of unsupported and supported IrO_x nanocatalysts.

Sample	IrO_x crystallite size (nm)	IrOx particle size (nm)
Unsupported IrO_x NPs	8.9	1.8 ± 0.4
IrO_x/TO	1.6	1.8 ± 0.4
IrO_x/ATO	1.9	1.7 ± 0.4
IrO_x/TaTO	1.9	1.7 ± 0.3

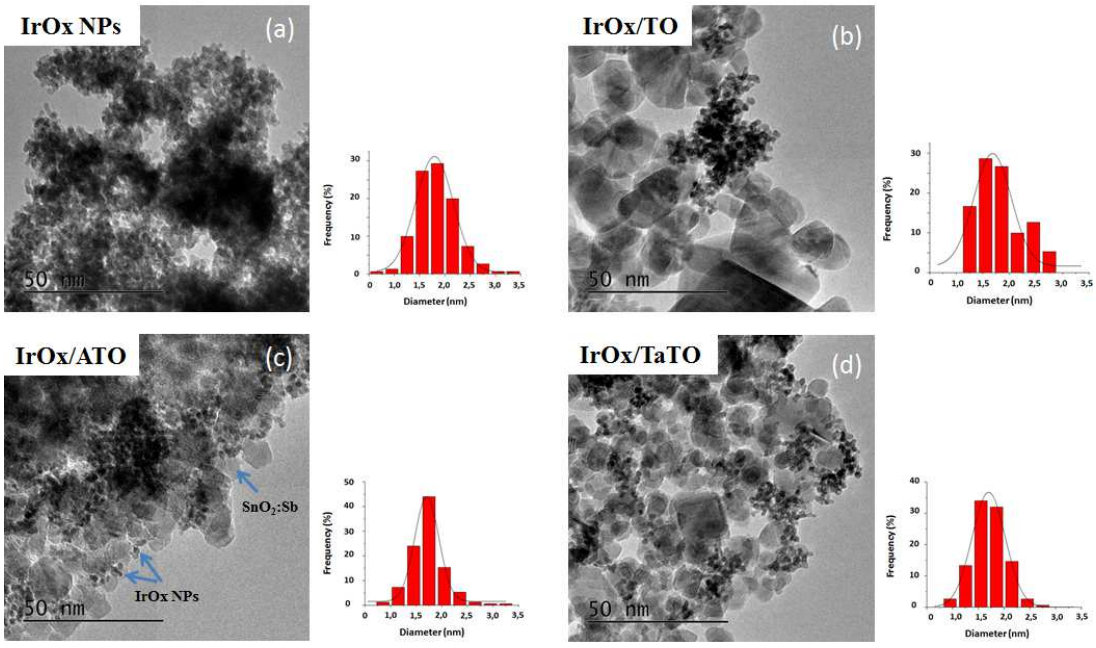

Figure 5. TEM images of (a) IrO_x NPs, (b) IrO_x/ TO, (c) IrO_x/ ATO and (d) IrO_x/TaTO and associated IrO_x particle size distribution.

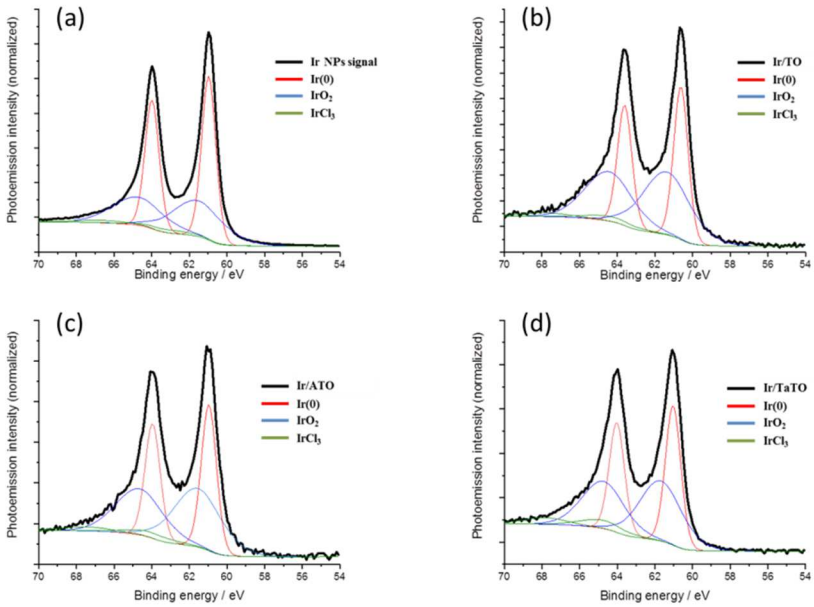

Figure 6. Detailed Ir 4f spectra of (a) IrO_x NPs, (b) IrO_x/TO, (c) IrO_x/ATO and (d) IrO_x/TaTO catalysts, showing the contribution of each Ir species.

Table 7. Bulk and surface chemical composition of the IrO_x/TO-based aerogels determined by EDX and XPS measurements.

Sample	Ir wt.% (EDX)	Ir wt.% (XPS)	Ir(0) at.% 60.8 eV ($4f_{7/2}$)	IrO_2 at.% 61.6 eV ($4f_{7/2}$)	IrClx at.% 62.9 eV ($4f_{7/2}$)
Unsupported IrO_x NPs	96.3 ± 2.4*	96.6 ± 2.5*	53.6 ± 5.9	42.6 ± 3.9	3.8 ± 1.4
IrO_x/TO	30 ± 1.3	30 ± 0.5	41.2 ± 4.0	49.9 ± 5.6	8.9 ± 2.4
IrO_x/ATO	29 ± 1.5	22 ± 0.3	42.7 ± 1.9	50.4 ± 1.9	6.9 ± 2.2
IrO_x/TaTO	33 ± 2.0	32 ± 0.9	41.9 ± 2.6	49.6 ± 2.5	8.6 ± 1.4

*complement to 100% with O and possibly Cl and/or C

Table 7 also shows that the IrO_x nanocatalysts are composed of both metallic Ir and Ir oxide in approximately the same amount. This was no surprise as nanocatalysts are prone to formation of an amorphous IrO_x layer (with $x < 2$) resulting from oxidation in air. The Ir4f peak was fitted using the parameters and the line shapes proposed by Freakley *et al.*[54] Three contributions were considered: metallic Ir(0), IrO_2 and $IrCl_3$. As shown in **Table 7**, the unsupported IrO_x NPs featured a higher Ir metallic content than the aerogel-supported IrO_x nanocatalysts. This higher metallic content mostly is a consequence of the larger particle size observed for this material. Regarding the deposited nanocatalysts over the TO aerogels, all IrO_x NPs present similar particle and crystallite sizes (**Table 6**), and similar metallic and oxide contributions, suggesting a crystalline metallic core and an amorphous oxide layer on the surface.

3.3 Electrocatalytic activity towards the OER and stability in acidic electrolyte

Finally, the OER activity of the four prepared catalysts was assessed using the protocol described in the experimental section. Conditioning of the electrodes was first carried out by performing a series of 10 cyclic voltammogram (CV) between 0.0 and 1.6 V *vs.* RHE and another of 3 CV cycles between 1.0 and 1.6 V. A 24 hour chronopotentiometry at 1 mA cm^{-2} was used to determine the stability of each catalyst under OER conditions.

The results, displayed in **Figure 7**, show a 5-fold and nearly 10-fold enhancement of the mass activity towards the OER on the aerogel-supported IrO_x NPs compared to unsupported IrO_x NPs at 1.51 V and 1.58 V, respectively. We related this to the effect of the IrO_x crystallite. Indeed, the size of the IrOx NPs is much smaller for supported than for unsupported catalysts, hence much higher density of sites is available to the reaction and faster OER kinetics result according to Butler-Volmer equation.The stability of the IrO_x NPs was also enhanced by the presence of the aerogel support, as the lifespan of the materials was improved from 1 hour for unsupported IrO_x NPs up to 17 hours for the IrO_x/TO catalyst (Figure 7.c and **Table 8**). Again, this is due to the smaller IrOx NP size. Indeed, due to smaller density of catalytic sites, the unsupported IrOx NPS are subjected to a higher overpotential during the chronopotentiometry (in order to be able to provide the requested current density), hence the lower durability observed.

Finally, we noticed that despite the different electronic conductivity of their supports (**Table 5**), similar geometric, mass and specific activities towards the OER were measured for the three aerogel-supported IrO_x catalysts. Even more surprising, IrO_x/TO was found to be the best-performing material. These results may however be rationalized by considering that, in RDE configuration, a very thin film of catalyst covers a glassy carbon disk with high electron-conductivity. As supported IrO_x/TO-based aerogel and carbon Fermi levels align upon contact, different OER activity are unlikely to translate when OER activities are determined in RDE

configuration. However, the situation will be very different for *ca*. 150-200-fold thicker PEMWE anodes, in which the electronic conductance of TO-based aerogels will be determined by their intrinsic conductivity, the resistance of their contacts, and the volume density of the latter. In that frame, it was no surprise to note that the time during which a current density of 1 mA cm^{-2} could be sustained (a cut-off voltage of 2 V was used) was almost not dependent of the nature of aerogel (**Table 8**). We thus conclude that quantifying the impact of the nature of the TO-based aerogel (undoped *vs*. Sb or Ta doped SnO_2) is hardly possible in RDE configuration.

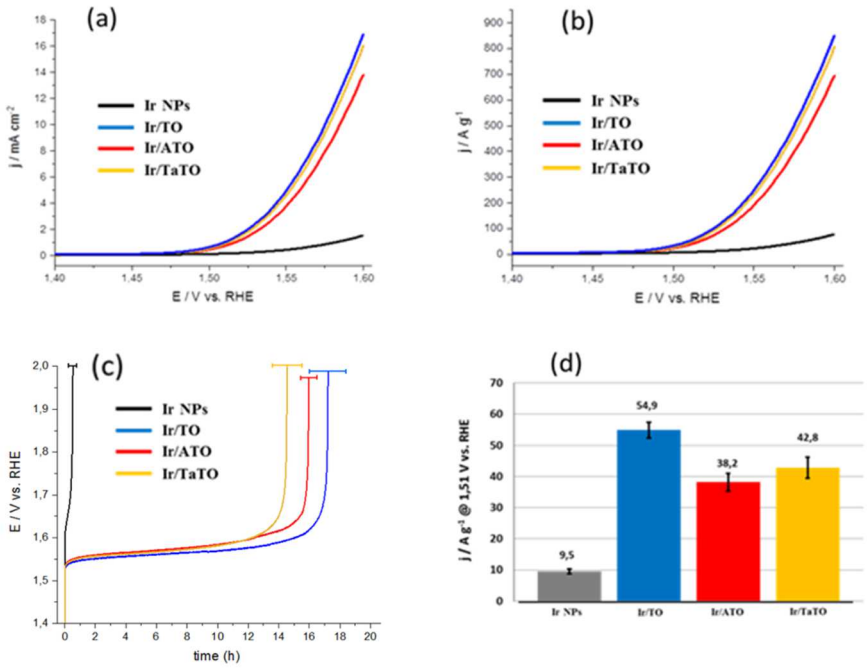

Figure 7. Electrocatalytic performance and durability of the as-prepared catalysts: (a) geometric activity (b) mass activity (c) stability at 1 mA/cm² and (d) mass activity comparison at an overpotential of 0.28 V. All measurements were performed at 25°C in N_2-saturated 0.05 M H_2SO_4 using a potential sweep rate of 5 mV s^{-1} and a rotation rate of 1600 rpm. The Ir loading was 20 µg cm^{-2} for all electrodes (3.9 µg Ir per RDE tip).

Table 8. Stability tests results for the synthesized catalysts (24 hour chronopotentiometry using a constant current density of 1 mA cm^{-2} and a cut-off voltage of 2.0 V.

Sample	Durability (@ 1 mA cm^{-2})
Unsupported IrO_x NPs	1.0 ± 0.5 h
IrO_x/TO	17.0 ± 2.5 h
IrO_x/ATO	16.0 ± 1.0 h
IrO_x/TaTO	14.5 ± 2.0 h

4. Conclusion

In conclusion, we showed that supporting IrO_x nanoparticles on tin oxide aerogels allows enhancing their OER activity and stability. Despite very different electronic conductivity, the OER mass and specific activities of IrO_x nanoparticles deposited onto tin oxide-based aerogels were found similar in thin-film electrode configuration. This is in agreement with the recent results obtained by the group of professor Uchida on different types of tin dioxide support. On top of a better OER activity, all aerogel supported IrO_x based catalysts also exhibited enhanced durability compared to unsupported IrO_x nanoparticles.

Also, since the morphology of tin dioxide based aerogels (TO, ATO and TaTO) is very similar to that of previously developed carbon aerogels, it is reasonable to think that the same fluid management benefits can be expected in real PEMWE device than we did observe in PEMFC. Considering the promising results reported in this study, we now aim at assessing their performance and durability in membrane electrodes assembly (MEA) where the impact of the support's electronic conductivity is key. Specific studies will also be carried out in order to optimize the doping element concentration as well as the Ir loading.

AUTHOR INFORMATION

Corresponding Authors

lluis.sola-hernandez@mines-paristech.fr

christian.beauger@mines-paristech.fr

Author Contributions

The manuscript was written through contributions of all authors.

Declarations of interest None

ACKNOWLEDGMENTS

The authors wish to thank Pierre Ilbizian for supercritical drying, Frédéric Georgi for XPS analysis, Suzanne Jacomet for SEM/EDX analysis and Gabriel Monge for XRD. This work was funded by the European Union's H2020 Program within the Fuel Cells and Hydrogen 2 Joint Undertaking under grant agreement 779478 (FCH-JU project PRETZEL) and the French National Research Agency (ANR-17-CE05-0033 project MOISE). It was supported by Capenergies and Tenerrdis.

REFERENCES

[1] Grigoriev SA, Porembsky V, Fateev VN, Pure hydrogen production by PEM electrolysis for hydrogen energy. Int. J. Hydrogen Energy, 2006; 31:171-75. https://doi.org/10.1016/j.ijhydene.2005.04.038

[2] Barbir F, PEM electrolysis for production of hydrogen from renewable energy sources. Sol. Energy, 2005; 78: 661-69. https://doi.org/10.1016/j.solener.2004.09.003

[3] Carmo M, Fritz DL, Mergel J, Stolten D, A comprehensive review on PEM water electrolysis, Int. J. Hydrogen Energy, 2013; 38: 4901-34. https://doi.org/10.1016/j.ijhydene.2013.01.151

[4] Siracusano S, Van Dijk N, Payne-Johnson E, Baglio V, Arico AS, Nanosized IrOx and IrRuOx electrocatalysts for the O2 evolution reaction in PEM water electrolysers, Appl. Catal. B, 2015; 164: 488-95. https://doi.org/10.1016/j.apcatb.2014.09.005

[5] Reier T, Oezaslan M, Strasser P, Electrocatalytic Oxygen Evolution Reaction (OER) on Ru, Ir, and Pt Catalysts: A Comparative Study of Nanoparticles and Bulk Materials , ACS Catal.2012; 2, 81: 765-1772. https://doi.org/10.1021/cs3003098

[6] Danilovic N, Subbaraman R, Chang KC, Chang SH, Kang Y, Snyder J, Paulikas AP, Strmcnik D, Kim YT, Myers D, Markovic N, Using Surface Segregation To Design Stable Ru-Ir Oxides for the Oxygen Evolution Reaction in Acidic Environments, Angew. Chem. Int. Ed., 2014; 53: 14016-21. https://doi.org/10.1002/anie.201406455

[7] Antolini E, Iridium As Catalyst and Cocatalyst for Oxygen Evolution/Reduction in Acidic Polymer Electrolyte Membrane Electrolyzers and Fuel Cells, ACS Catal., 2014; 4: 1426-40. https://doi.org/10.1021/cs4011875

[8] Seitz L, Dickens C, Nishio K, Hikita Y, Montoya J, Doyle A, Kirk C, Vojvodic A, Hwang H, Norskov J, Jaramillo T, A highly active and stable IrOx/SrIrO3 catalyst for the oxygen evolution reaction, Science, 2016; 353: 1011-14. https://doi.org/10.1126/science.aaf5050

[9] Nong HN, Oh HS, Reier T, Willinger E, Willinger MG, Petkov V, Teschner D, Strasser P, Oxide-Supported IrNiOx Core–Shell Particles as Efficient, Cost-Effective, and Stable Catalysts for Electrochemical Water Splitting, Angew. Chem. Int. Ed., 2015; 54: 2975-79 https://doi.org/10.1002/anie.201411072

[10]Dicks AL, The role of carbon in fuel cells, J. Power Sources, 2006; 156: 128-41. https://doi.org/10.1016/j.jpowsour.2006.02.054

[11] Antolini E, Gonzalez ER, Polymer supports for low-temperature fuel cell catalysts, Appl. Catal. A, 2009; 365: 1-19. https://doi.org/10.1016/j.apcata.2009.05.045

[12] Antolini E, Graphene as a new carbon support for low-temperature fuel cell catalysts, Appl. Catal. B, 2012; 123: 52-68. https://doi.org/10.1016/j.apcatb.2012.04.022

[13] Oh HS, Kim K, Kim H, Polypyrrole-modified hydrophobic carbon nanotubes as promising electrocatalyst supports in polymer electrolyte membrane fuel cells, Int. J. Hydrogen Energy, 2011; 36: 11564-71. https://doi.org/10.1016/j.ijhydene.2011.06.079

[14] Huang H, Chen S, Yuan C, Platinum nanoparticles supported on activated carbon fiber as catalyst for methanol oxidation, J. Power Sources, 2008; 175: 166-74. https://doi.org/10.1016/j.jpowsour.2007.08.107

[15] Yu X, Ye S, Recent advances in activity and durability enhancement of Pt/C catalytic cathode in PEMFC: Part I. Physico-chemical and electronic interaction between Pt and carbon support, and activity enhancement of Pt/C catalyst, J. Power Sources, 2007; 172: 133-44. https://doi.org/10.1016/j.jpowsour.2007.07.049

[16] Oh HS, Lim KH, Roh B, Hwang I, Kim H, Corrosion resistance and sintering effect of carbon supports in polymer electrolyte membrane fuel cells, Electrochim. Acta, 2009; 54: 6515-21. https://doi.org/10.1016/j.electacta.2009.06.028

[17] Oh HS, Oh JG, Haam S, Arunabha K, Roh B, Hwang I, Kim H, On-line mass spectrometry study of carbon corrosion in polymer electrolyte membrane fuel cells, Electrochem. Commun., 2008; 10: 1048-51. https://doi.org/10.1016/j.elecom.2008.05.006

[18] Maass S, Finsterwalder F, Frank G, Hartmann R, Merten CJ, Carbon support oxidation in PEM fuel cell cathodes, J. Power Sources, 2008; 176: 444-51. https://doi.org/10.1016/j.jpowsour.2007.08.053

[19] Claudel F, Dubau L, Berthomé G, Sola-Hernandez L, Beauger C, Piccolo L, Maillard F, Degradation Mechanisms of Oxygen Evolution Reaction Electrocatalysts: A Combined Identical-Location Transmission Electron Microscopy and X-ray Photoelectron Spectroscopy Study, ACS Catal. ,2019; 9(5): 4688-98. https://doi.org/10.1021/acscatal.9b00280

[20] Antolini E, Gonzalez ER, Ceramic materials as supports for low-temperature fuel cell catalysts, Solid State Ionics, 2009; 180: 746-63. https://doi.org/10.1016/j.ssi.2009.03.007

[21] Lu Y, Jiang Y, Gao X, Wang X, Chen W, Strongly Coupled Pd Nanotetrahedron/Tungsten Oxide Nanosheet Hybrids with Enhanced Catalytic Activity and Stability as Oxygen Reduction Electrocatalysts, J. Am. Chem. Soc., 2014; 136: 11687-97. https://doi.org/10.1021/ja5041094

[22] Luo F, Liao S, Dang D, Zheng Y, Xu D, Nan H, Shu T, Fu Z, Tin and Silicon Binary Oxide on the Carbon Support of a Pt Electrocatalyst with Enhanced Activity and Durability, ACS Catal., 2015; 5: 2242-49. https://doi.org/10.1021/cs501429g

[23] Resasco D, Haller GL, A model of metal-oxide support interaction for Rh on TiO2, J. Catal., 1983; 82: 279-88. https://doi.org/10.1016/0021-9517(83)90194-X

[24] Huang S, Ganesan P, Park S, Popov BN, Development of a Titanium Dioxide-Supported Platinum Catalyst with Ultrahigh Stability for Polymer Electrolyte Membrane Fuel Cell Applications, J. Am. Chem. Soc., 2009; 131: 13898-99. https://doi.org/10.1021/ja904810h

[25] Liu Y, Mustain WE, High Stability, High Activity Pt/ITO Oxygen Reduction Electrocatalysts, J. Am. Chem. Soc., 2013; 135:530-33. https://doi.org/10.1021/ja307635r

[26] Wang L, Lettenmeier P, Golla-Schindler U, Gazdzicki P, Canas N, Morawietz T, Hiesgen R, Hosseiny R, Gago A, Friedrich K, Nanostructured Ir-supported on Ti4O7 as a cost-effective anode for proton exchange membrane (PEM) electrolyzers, Phys. Chem. Chem. Phys., 2016; 18: 4487-95. https://doi.org/10.1039/C5CP05296C

[27] Chen G, Bare SR, Mallouk TE, Development of Supported Bifunctional Electrocatalysts for Unitized Regenerative Fuel Cells, J. Electrochem. Soc., 2002 ;149: 1092 - 99. https://doi.org/10.1149/1.1491237

[28]Siracusano S, Baglio V, .D'Urso C, Antonucci V, Aricò A.S, Preparation and characterization of titanium suboxides as conductive supports of IrO2 electrocatalysts for application in SPE electrolysers, Electrochemical Acta, 2009; 54 (26): 6292-6299. https://doi.org/10.1016/j.electacta.2009.05.094

[29] Puthiyapura K.V, Pasupathi S, Su H, Liu X, Pollet B, Scott K, Investigation of supported IrO2 as electrocatalyst for the oxygen evolution reaction in proton exchange membrane water electrolyser, International Journal of Hydrogen Energy, 2014; 39 (5): 1905-1913. https://doi.org/10.1016/j.ijhydene.2013.11.056

[30] Kotz R, Stucki S, Carcer B, Electrochemical waste water treatment using high overvoltage anodes. Part I: Physical and electrochemical properties of SnO2 anodes, J. Appl. Electrochem., 1991; 21: 14-20. https://doi.org/10.1007/BF01103823

[31] Oh H, Nong HN, Strasser P, Preparation of Mesoporous Sb-, F-, and In-Doped SnO2 Bulk Powder with High Surface Area for Use as Catalyst Supports in Electrolytic Cells, Adv. Funct. Mater., 2015; 25: 1074-81. https://doi.org/10.1002/adfm.201401919

[32] Vicent F, Morallon E, Quijada E, Vazquez JL, Aldaz A, Cases F, Characterization and stability of doped SnO2 anodes, J. Appl. Electrochem., 1998; 28: 607-12. https://doi.org/10.1023/A:1003250118996

[33] Puthiyapura VK, Mamlouk M, Pasupathi S, Pollet BG, Scott K, Physical and electrochemical evaluation of ATO supported IrO2 catalyst for proton exchange membrane water electrolyzer, J. Power Sources, 2014; 269: 451-460. https://doi.org/10.1016/j.jpowsour.2014.06.078

[34] Oh H, Nong HN, Teschner D, Reier T, Bergmann A, Gliech M, Ferreira de Araujo J, Willinger E, Schlogl R, Teschner D, Strasser P, Electrochemical Catalyst–Support Effects and Their Stabilizing Role for IrOx Nanoparticle Catalysts during the Oxygen Evolution Reaction, J. Am. Chem. Soc., 2016; 138: 12552-63. https://doi.org/10.1021/jacs.6b07199

[35] Wang L, Song F, Ozouf G, Geiger D, Morawietz T, Handl M, Gazdzicki P, Beauger C, Kaiser U, Hiesgen R, Gago AS, Friedrich KA, Improving the activity and stability of Ir catalysts for PEM electrolyzer anodes by SnO2:Sb aerogel supports: does V addition play an active role in electrocatalysis?, J. Mater. Chem. A, 2017; 5: 3172-78. https://doi.org/10.1039/C7TA00679A

[36] Ozouf G, Beauger C, Niobium- and antimony-doped tin dioxide aerogels as new catalyst supports for PEM fuel cells, J. Mater. Sci., 2016; 51: 5305-20. https://doi.org/10.1007/s10853-016-9833-7

[37] Senoo Y, Taniguchi K, Kakinuma K, Uchida M, Uchida H, Deki S, Watanabe M, Cathodic performance and high potential durability of Ta-SnO2 − δ-supported Pt catalysts for PEFC cathodes, Electrochemistry Communications, 2015; 51: 37-40. https://doi.org/10.1016/j.elecom.2014.12.005

[38] Fabbri E, Rabis A, Chino Y, Uchida U, Schmidt TJ, Boosting Pt oxygen reduction reaction activity by tuning the tin oxide support, Electrochemistry Communications, 2017; 83; 90-95. https://doi.org/10.1016/j.elecom.2017.09.006

[39] Fabbri E, Rabis A, Kotz R, Schmidt TJ, Pt nanoparticles supported on Sb-doped SnO2 porous structures: developments and issues, Phys.Chem.Chem.Phys., 2014; 16: 13672-81. https://doi.org/10.1039/C4CP00238E

[40] Ohno H, Nohara S, Kakinuma K, Uchida M, Uchida H, Effect of Electronic Conductivities of Iridium Oxide/Doped SnO2 Oxygen-Evolving Catalysts on the Polarization Properties in Proton Exchange Membrane Water ElectrolysisCatalysts, 2019; 9; 74-86. https://doi.org/10.3390/catal9010074

[41] Thomas, I.M., Method for producing stannic tertiary alkoxide. 1976, Google Patents

[42] Reier T, Pawolek Z, Cherevko S, Bruns M, Jones T, Teschner D, Selve S, Bergmann A, Nong HN, Schlögl HR, Mayrhofer KJJ, Strasser P, Molecular Insight in Structure and Activity of Highly Efficient, Low-Ir Ir–Ni

Oxide Catalysts for Electrochemical Water Splitting (OER), J. Am. Chem. Soc., 2015; 137: 13031-40. https://doi.org/10.1021/jacs.5b07788

[43] Ardizzone S, Fregonara G, Trasatti S, “Inner” and “outer” active surface of RuO2 electrodes, Electrochim. Acta, 1190; 35: 263-67. https://doi.org/10.1016/0013-4686(90)85068-X

[44] Ouattara-Brigaudet M, Beauger C, Berthon-Fabry S, Achard P, Carbon Aerogels as Catalyst Supports and First Insights on Their Durability in Proton Exchange Membrane Fuel Cells, Fuel Cells, 2011; 11 (6): 726-34. https://doi.org/10.1002/fuce.201000182

[45] Baur WH, Über die Verfeinerung der Kristallstrukturbestimmung einiger Vertreter des Rutiltyps: TiO2, SnO2, GeO2 und MgF2, Acta Crystallographica, 1956; 9: 515-20. https://doi.org/10.1107/S0365110X56001388

[46] Cognard G, Ozouf G, Beauger C, Berthomé G, Riasetto D, Dubau L, Chattot R, Chatenet M, Maillard F, Benefits and limitations of Pt nanoparticles supported on highly porous antimony-doped tin dioxide aerogel as alternative cathode material for proton-exchange membrane fuel cells, Appl. Cat. B., 2017; 201: 381-90. https://doi.org/10.1016/j.apcatb.2016.08.010

[47] Cognard G, Ozouf G, Beauger C, Jiménez-Morales I, Cavaliere S, Jones D, Rozière J, Chatenet M, Maillard F, Pt nanoparticles supported on niobium-doped tin dioxide: impact of the support morphology on Pt utilization and electrocatalytic activity, Electrocatalysis, 2017; 8: 51-58. https://doi.org/10.1007/s12678-016-0340-Z

[48] Cognard G, Ozouf G, Beauger C, Dubau L, López-Haro M, Chatenet M, Maillard F, Insights into the stability of Pt nanoparticles supported on antimony-doped tin oxide in different potential ranges, Electrochim. Acta, 2017; 245: 993-1004. https://doi.org/10.1016/j.electacta.2017.05.178

[49] Ozouf G, Cognard G, Maillard F, Chatenet M, Guétaz L, Heitzmann M, Jacques PA, Beauger C, Sb-Doped SnO 2 Aerogels Based Catalysts for Proton Exchange Membrane Fuel Cells: Pt Deposition Routes, Electrocatalytic Activity and Durability, Journal of the Electrochimical Society, 2018; 165 (6): 3036-44. https://doi.org/10.1149/2.0041806jes

[50] Beauger C, Testut L, Berthon-Fabry S, Georgi F, Guétaz L, Doped TiO2 aerogels as alternative catalyst supports for proton exchange membrane fuel cells: A comparative study of Nb, V and Ta dopants, Microporous and Mesoporous Materials, 2016; 232: 109-118. https://doi.org/10.1016/j.micromeso.2016.06.003

[51] Abbott D, Lebedev D, Waltar K, Povia M, Nachtegaal M, Fabbri E, Copéret C, Schmidt TJ, Iridium Oxide for the Oxygen Evolution Reaction: Correlation between Particle Size, Morphology, and the Surface Hydroxo Layer from Operando XAS, Chem. Mater., 2016; 28: 6591-6604. https://doi.org/10.1021/acs.chemmater.6b02625

[52] Bruneaux J, Cachet H, Froment M, Messad A, Structural, electrical and interfacial properties of sprayed SnO2 films, Electrochimica Acta, 1994; 39: 1251-57. https://doi.org/10.1016/0013-4686(94)E0044-Z

[53] Wyckoff RWG. (1963). *Crystal Structures - Volume 1*. New York: Interscience Publishers

[54] Freakley S, Ruix-Esquius J, Morgan D, The X-ray photoelectron spectra of Ir, IrO2 and IrCl3 revisited, Surf. Interface Anal., 2017; 49: 794-99. https://doi.org/10.1002/sia.6225